Origin of enhanced nonradiative carrier recombination induced by oxygen in hybrid Sn perovskite

Yuhang Liang,[1,2] *Xiangyuan Cui*,[3,*] *Feng Li*,[2] *Catherine Stampfl*,[2] *Simon P. Ringer*,[3] *Xudong Yang*,[4,5,6] *Jun Huang*,[1,*] *Rongkun Zheng*[2,*]

[1] School of Chemical and Biomolecular Engineering, The University of Sydney, NSW 2006, Australia

[2] School of Physics, The University of Sydney, NSW 2006, Australia

[3] School of Aerospace, Mechanical and Mechatronic Engineering, The University of Sydney, NSW 2006, Australia

[4] State Key Laboratory of Metal Matrix Composites, Shanghai Jiao Tong University, Shanghai 200240, China

[5] Center of Hydrogen Science, School of Materials Science and Engineering, Shanghai Jiao Tong University, Shanghai 200240, China

[6] Zhangjiang Institute for Advanced Study, Shanghai Jiao Tong University, Shanghai 201210, China

*Xiangyuan Cui: carl.cui@sydney.edu.au

*Jun Huang: jun.huang@sydney.edu.au

*Rongkun Zheng: rongkun.zheng@sydney.edu.au

Abstract

Oxygen ingression has been shown to substantially decrease the carrier lifetime of Sn-based halide perovskites by accelerating the nonradiative recombination, behind which the mechanism at the atomic scale remains yet unknown. Our first-principles calculations reveal that in prototypical $MASnI_3$ ($MA=CH_3NH_3$), oxygen by itself is not responsible for the nonradiative recombination. Instead, it tends to form substitutional O_I through interacting strongly with abundant native I vacancies (V_I). The formation of O_I remarkably increases the original nonradiative recombination rate of V_I by two to

three orders of magnitude, rationalizing the experimentally observed sharp decline of carrier lifetime in perovskites exposed to air. The significantly enhanced carrier recombination is due to a smaller electron capture barrier of O_I, resulting from lattice strengthening and the suppressed structural relaxation associated with the charge-state transition. These insights offer a route to further improve device performance via anion engineering in broad Sn-based perovskite optoelectronics operating in ambient air. Moreover, our results highlight the important role of lattice relaxation for nonradiative carrier capture in materials in general.

Keywords Sn halide perovskites, oxygen, nonradiative recombination, lattice relaxation

Introduction

Hybrid perovskites have recently attracted intense interest in optoelectronics due to their outstanding photophysical properties and low processing cost. The power conversion efficiencies (PCE) of perovskite solar cells have skyrocketed up to over 25% within a decade[1–3], surpassing that of the present photovoltaic market leader polycrystalline silicon. However, there are still challenges facing the successful commercialization of perovskite solar cells.

One critical negative aspect is the high vulnerability to the ambient air, particularly for Sn-based halide perovskites, which alleviate the health and environmental hazards raised by the Pb-based counterparts and deliver superior semiconductor properties such as the nearly-ideal bandgaps and higher absorption coefficients[4]. The performance of solar cells without encapsulation deteriorates rapidly in the air with the carrier lifetime being significantly reduced to that far below practical requirements[5]. Experimental reports indicate that atmospheric oxygen plays an important role in degrading the Sn-based perovskite active layers and substantially enhances the nonradiative charge recombination[6–9], which is the main cause of energy loss in perovskite photovoltaics[10,11]. Therefore, numerous efforts have been devoted to preventing oxygen diffusion into the Sn-based perovskite devices, such as via encapsulation[12], the introduction of the larger

organic cations[13], and antioxidant additives[5]. However, these approaches fall short of fully addressing the issue due to uncontrollable oxygen leakage during fabrication and operation[8]. Indeed, Sn-based perovskite devices are typically required to be processed under extremely low oxygen concentration conditions (less than 0.1 ppm)[14], which significantly restricts scalable and industrial production. To date, the atomic-scale mechanism underlying oxygen (air) exposure accelerating nonradiative carrier recombination in Sn-based perovskites remains poorly understood, and a full elucidation is key to developing accurate remedial strategies as well as the further design of efficient Sn-based perovskite solar cells and other broad device applications under ambient air operation.

In this study, by performing accurate first-principles hybrid density functional calculations, we report that in the prototypical Sn-based perovskite $MASnI_3$ ($MA=CH_3NH_3$), though oxygen can be readily incorporated into the lattice, it cannot cause nonradiative recombination by itself. Instead, oxygen atoms tend to be trapped into the native I vacancies (V_I) and form substitutional O_I as the dominant defect species. V_I acts as a dominant nonradiative recombination center, of which the capture of electrons is the rate-limiting step in $MASnI_3$. Our results show that the formation of O_I significantly accelerates the electron capture process and thus increases the overall nonradiative recombination rate further by two to three orders of magnitude. These results rationalize the observed sharp decline of carrier lifetime in perovskite active layers exposed to oxygen (air). In addition, contrary to the conventional notion that the carrier capture rate often declines exponentially with the transition energy, the results show that the formation of O_I actually leads to enhanced electron transition energy. Notably, the formation of O_I strengthens the lattice and reduces the structural relaxation upon electron capture, which plays an important role in decreasing the electron capture barrier, responsible for a substantially enhanced nonradiative recombination rate.

Results and Discussion

To evaluate the impact of oxygen (O) on nonradiative recombination in Sn-based perovskites, we first analyzed the thermodynamic stability of O within the lattice of the prototypical hybrid Sn perovskite $MASnI_3$ ($MA= CH_3NH_3$). **Figure 1a** shows the calculated formation energies of atomic oxygen (O_i) and molecular oxygen (O_2) in the

interstice of $MASnI_3$, as a function of the Fermi level within the bandgap. Both O_i and O_2 exhibit relatively low formation energies, especially for the negative values of the Fermi level in the proximity of the conduction band minimum (CBM). This indicates that oxygen impurities can be present in bulk $MASnI_3$ with a high density, once exposed to ambient air.

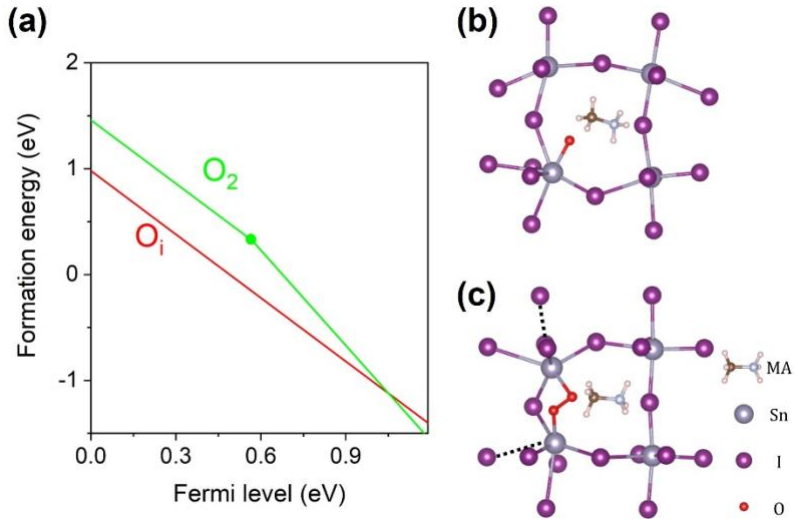

Figure 1. (a) Formation energies of interstitial atomic and molecular oxygen in $MASnI_3$ as a function of the Fermi level. The local atomic structures of (b) O_i^{2-} and (c) O_2^{2-} in $MASnI_3$.

In $MASnI_3$, O_i tends to capture extra electrons as expected for a completely full *p* orbital leading to the formation of the negatively charged O_i^{2-} located next to the host Sn cation, as shown in **Figure 1b**. The O-bonded Sn is displaced toward the oxygen atom from the original position, and the nearby I atoms are repelled outward, resulting in local structural distortion, which can be attributed to the high ionic and soft lattice characteristics of halide perovskite materials. For O_2, as shown in **Figure 1c**, each oxygen atom of the molecule tends to bind with the neighboring Sn cations leading to the puckered Sn-I-Sn framework, which implies that both oxygen atoms in O_2 are slightly negatively charged. Indeed, O_2 in the bulk of $MASnI_3$ has a longer molecular bond length of 1.60 Å, compared with 1.21 Å for free O_2, making it more like an oxygen dimer. According to the Shockley−Read−Hall theory of recombination[15], the presence

of a deep trap state (charge-state transition level) in the bandgap is a prerequisite for defects that serve as nonradiative recombination centers. O_2 induces a deep transition level of $\varepsilon(-2/-3)$ (~0.57 eV above the valance band maximum (VBM), whereas its formation energy is higher than that of O_i over the wide range of the Fermi level within the bandgap. This, therefore, suggests that O_2 can be unstable within the lattice of $MASnI_3$ and tends to disassociate into the isolated O_i under equilibrium conditions (also see the positive binding energies of O_2 with respect to two isolated O_i in **Table S1**). On the other hand, O_i is stable in -2 charged state throughout the Fermi level with the transition level $\varepsilon(0/-2)$ being located at 0.21 eV below the VBM, namely a shallow acceptor, and thus cannot act as the charge carrier recombination center.

Table 1. Calculated binding energy of the oxygen interstitial O_i^{2-} with the three types of native vacancies.

Site	V_I^+	V_I^-	V_{Sn}^{2-}	V_{MA}^-
Binding energy (eV)	-1.06	0.72	0.95	0.24

It was experimentally reported that oxygen exposure leads to enhanced nonradiative charge carrier recombination in hybrid Sn perovskites[6–9], significantly reducing carrier lifetime and deteriorating the device performance. However, the present results indicate that oxygen interstitials are not responsible for the recombination center by themselves. To understand the role of oxygen incorporation in nonradiative recombination in Sn-based perovskites, we further considered the potential interactions of oxygen and native vacancies that usually exhibit low formation energies in halide perovskite materials[16] and could be the preferred lattice sites for incorporated oxygen. We thus calculated the binding energies of O_i^{2-} with three typical native vacancies, namely, V_I^+ (V_I^-), V_{Sn}^{2-}, and V_{MA}^-, respectively, as shown in **Table 1**. The results imply that, besides isolated O_i^{2-} ions, there exist other dominant forms of oxygen in $MASnI_3$: isolated oxygen interstitial O_i^{2-} can interact strongly with native V_I^+, resulting in the formation of a substitutional defect made of oxygen trapped into an I vacancy, namely, O_I^-. Further, placing a second O_i^{2-} into vacancy is energetically unfavorable with the calculated binding energy of 0.78 eV, which can be attributed to anionic Coulomb

repulsion.

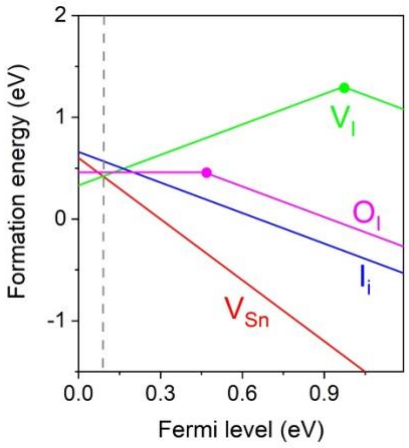

Figure 2. Calculated formation energies of three low-energy native defects (V_{Sn}, V_I, and I_i) and O_I of the dominant form of oxygen in $MASnI_3$ under typical moderate growth conditions. The vertical dashed line stands for the location at which the Fermi level is pinned, based on the condition of charge neutrality between the lowest-energy defects.

Figure 2 shows the formation energies of the three energetically most favorable native defects as well as that of O_I as a function of the Fermi level in $MASnI_3$. These three lowest-energy native defects are the Sn vacancy (V_{Sn}), I vacancy (V_I) and I interstitial (I_i)[17,18]. V_{Sn} is the lowest-energy native defect in $MASnI_3$ and stands as a robust shallow acceptor. Previous studies indicate that I_i is a highly efficient nonradiative recombination center in Pb-based perovskites[19–22]; nevertheless, in the case of $MASnI_3$, I_i only exhibits the negatively charged state (-1), that is, a shallow acceptor. Notably for V_I, the neutral-state V_I^0 is energetically less favorable than either the positively charged V_I^+ and negatively charged V_I^- over the entire Fermi-level range, resulting in a deep transition energy level of $\varepsilon(+/-)$ being 0.22 below the CBM (the intersection of the formation energies of V_I^+ and V_I^-), which is characteristic of a so-called negative-U behavior. The results show that V_I and O_I are two deep-level defects in $MASnI_3$.

For the negative-U center V_I, $\varepsilon(+/-)$ is expected not to govern the nonradiative recombination process even though it is deep in the bandgap, since a defect does not

capture simultaneously two electrons or holes. Effective carrier recombination typically involves single-charge-state transitions, namely, $\varepsilon(+/0)$ and $\varepsilon(0/-)$. As shown in **Figure 3a**, for V_I, $\varepsilon(+/0)$ is a shallow level located within the conduction band, and $\varepsilon(0/-)$ is a deep level being 0.71 eV above the VBM, hence is a relevant transition level for nonradiative recombination. Notably, after oxygen incorporation leading to the formation of O_I, it still possesses the deep-level characteristic and the $\varepsilon(0/-)$ level moves closer to the VBM (0.46 eV above the VBM).

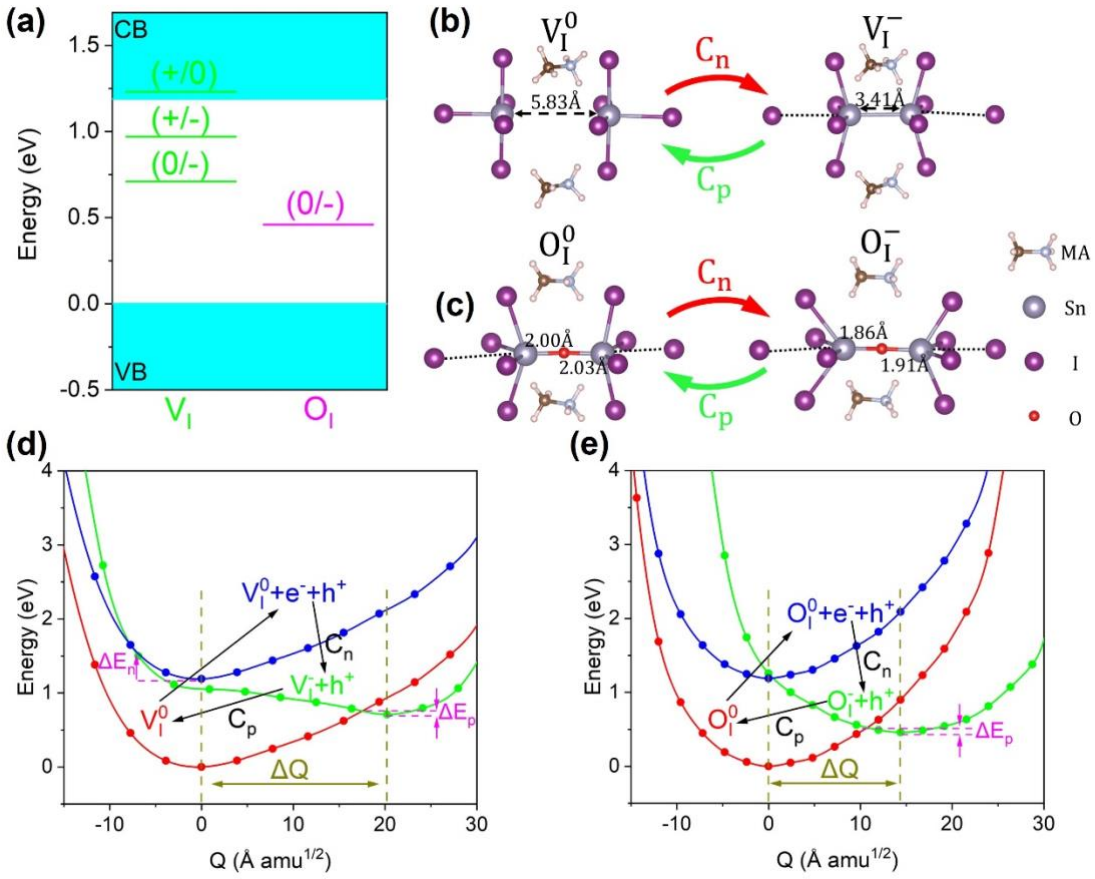

Figure 3. (a) Thermodynamic ionization levels of V_I and O_I in $MASnI_3$ calculated with the HSE-SOC-TS scheme. Local atomic structures of (b) V_I and (c) O_I in the two relevant charge states (0 and −), where the arrows and labels stand for the relevant carrier capture processes. Configuration coordinate diagrams for the charge-state transitions of (d) $V_I^0 \leftrightarrow V_I^-$ and (e) $O_I^0 \leftrightarrow O_I^-$ in $MASnI_3$ as a function of a generalized configuration coordinate (Q).

To explicitly assess the effect of deep-level V_I and O_I in nonradiative recombination, we studied the related carrier capture processes by following the established multiphonon emission methodology[23,24]. **Figures 3b and 3c** show the local atomic structures of V_I and O_I in the two related charged states, namely 0 and –, respectively. For the neutral V_I^0 (**Figure 3b**), the removal of the I atom results in a slight lattice contraction with the distance between two nearby Sn being 5.83 Å, compared with 6.22 Å for the perfect system. By capturing an electron (C_n), V_I^0 transforms into V_I^- with two nearby Sn moving closer to the vacancy site leading to the formation of an Sn dimer, which is known as a DX center, as reported in $MAPbI_3$[25,26]. Subsequently, the negatively charged V_I^- can capture a hole (C_p) and relax back to the neutral V_I^0. Similarly, the transition of $O_I^0 \leftrightarrow O_I^-$ involves two carrier capture processes (electron capture C_n and hole capture C_p), as shown in **Figure 3c**. O occupies the center of I vacancy in both charge states and reduces the neighboring Sn-Sn distances, especially in the case of O_I^-.

We further calculated the configuration coordinate diagrams (CCD) for the transitions of $V_I^0 \leftrightarrow V_I^-$ and $O_I^0 \leftrightarrow O_I^-$, as shown in **Figures 3d and e**, which not only provides an intuitive illustration of a complete cycle of nonradiative carrier capture, but also derives the important input parameters for further nonradiative coefficient calculations[24]. The CCD maps the potential energy surfaces (PESs) of the related charge-state transitions as a function of a generalized coordinate (Q), which reflects the geometric differences with respect to a reference configuration. Semiclassically, each carrier capture process requires overcoming kinetic barriers, which is the energy required to cross the intersection of the PESs between the initial and final charge states in the CCD and hence determines the capture rates.

As shown in **Figure 3d**, for a V_I^0 with an electron at the CBM and a hole at the VBM (blue line), the energy barrier for electron captured by V_I^0 (the intersection between the blue and green lines) is markedly larger ($\Delta E_n \sim 0.31$ eV) than that of the hole capture process by V_I^- (the intersection between the green line and red line, $\Delta E_h \sim 0.08$ eV), indicative of faster hole capture. On the other hand, the slower electron capture process can be the rate-limiting step in the overall nonradiative cycle. In the case of the carrier recombination process in O_I (**Figure 3e**), the hole capture process exhibits a similar kinetic barrier ($\Delta E_h \sim 0.05$ eV) as that for V_I, while the electron capture barrier is almost

zero, since the PES of O_I^- (green line) almost goes through the minimum of the PES of O_I^0 (blue line).

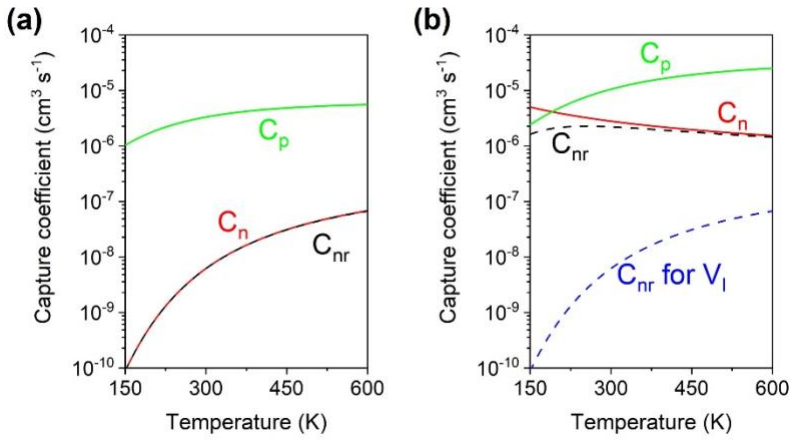

Figure 4. Nonradiative electron (red solid line) and hole (green solid line) capture, and recombination (black dashed line) coefficients of (a) V_I and (b) O_I in $MASnI_3$ as a function of temperature.

We then quantitively calculated the nonradiative carrier capture coefficients based on the strength of the electron-phonon coupling and the vibronic overlap between PESs. As shown in **Figure 4a**, consistent with the semiclassical CCD analysis, for V_I, the hole capture coefficient (C_p) is significantly higher than that for the electron (C_n) (around three orders of magnitude difference at room temperature). Additionally, the electron capture coefficient (C_n) exhibits a much faster enhancement trend with temperature (T) compared with C_p, which can be attributed to the higher electron capture barrier. The carrier capture is a thermally activated process and therefore higher kinetic energy generally results in a stronger positive temperature dependence.

Based on the balance between electron and hole captures under steady-state conditions[27], the nonradiative carrier recombination coefficient C_{nr} can be given by $C_{nr} = \frac{C_n C_p}{C_n + C_p}$. At room temperature (i.e. 300 K), the nonradiative carrier recombination coefficient of V_I in $MASnI_3$ is 6.2×10^{-9} cm^3 s^{-1}, which is similar to that of I_i in $MAPbI_3$ ($C_{nr} \sim 7 \times 10^{-9}$ cm^3 s^{-1})[19] that has been demonstrated to be the dominant nonradiative recombination center impacting the $MAPbI_3$-based device performance.

This indicates that V_I is likely the dominant native nonradiative recombination center in $MASnI_3$.

In the case of O_I, as shown in **Figure 4b**, the hole capture coefficient is comparable to that of V_I, consistent with the similar kinetic barriers predicted in the CCD. In contrast, the electron capture process exhibits a much higher capture coefficient with the C_n being up to $2.8 \times 10^{-6}\ cm^3\ s^{-1}$ at room temperature. Correspondingly, the nonradiative carrier recombination coefficient of O_I is up to $C_{nr} = 2.2 \times 10^{-6}\ cm^3\ s^{-1}$ at room temperature.

The nonradiative recombination rate constant A, also known as the Shockley-Read-Hall (SRH) rate constant, hence can be obtained jointly by the defect density (N) and the nonradiative capture coefficient per defect (C_{nr}), yielding $A = N \times C_{nr}$[27], which represents the number of nonradiative recombination events per unit time, i.e., the reciprocal of nonradiative carrier lifetime τ_{nr}.

In $MASnI_3$, V_{Sn} serves as the lowest-energy acceptor and V_I as the lowest-energy donor even with O being incorporated into the material; thus, the Fermi level largely is pinned by V_{Sn} and V_I, at around 0.14 eV above the VBM, as depicted by the gray dashed line in **Figure 2**. This is consistent with the experimentally observed *p*-type conductivity behavior in the $MASnI_3$ samples[28]. Under this condition, V_I and O_I exhibit similar formation energies. According to the thermal equilibrium equation, the densities (N) of V_I and O_I are estimated to be $1.5 \times 10^{15}\ cm^{-3}$ and $0.8 \times 10^{15}\ cm^{-3}$ at room temperature, respectively.

Without oxygen ingression, the SRH rate constant A induced by native V_I is $9.3 \times 10^6\ s^{-1}$. Exposure to ambient air (oxygen) leads to the formation of O_I, whose $C_{nr} = 2.2 \times 10^{-6}\ cm^3\ s^{-1}$, and the SRH rate constant A increases to $1.8 \times 10^9\ s^{-1}$. Such a significant enhancement of the nonradiative recombination rate constant implies an appreciable reduction of the carrier lifetime by around two to three orders of magnitude, which provides a rationale for the experimental fact that oxygen exposure results in a rapid decline of carrier lifetime and power conversion efficiency in $MASnI_3$-based devices[6,7]. Indeed, the SRH rate constant of O_I is close to the experimentally reported values, typically on the order of $10^9\ s^{-1}$ for $MASnI_3$ samples[29–31].

We noted that the capture of the electron serves as the rate-limiting process for the

nonradiative carrier recombination for V_I and O_I. With O incorporation resulting in forming O_I, the electron capture process is significantly accelerated, which is thus responsible for a higher overall nonradiative recombination rate. However, the calculations show that the formation of O_I shifts the position of the $\varepsilon(0/-)$ level down with a larger electron transition energy, compared with the original V_I (**Figure 3a**). This is in contrast to the traditional notion that the carrier capture rate generally decreases exponentially with the depth of transition energy[32] (the energy difference between the transition level and the corresponding band edges; the CBM for electron and the VBM for hole). Such a counterintuitive behavior can be attributed to two other important effects associated with lattice strain.

First, the incorporated O in V_I can form a stronger ionic Sn-O-Sn bond even than the metallic Sn-Sn bond with V_I^- and thus reduces the softness of the lattice. The lattice strengthening recovers the harmonicity (parabola) of the potential energy surface of O_I^- compared with the case of V_I^- (green lines in **Figures 3d 3e**), which thus pushes the system into the so-called Marcus inverted region[33] (the PESs intersect within $0 < Q < \Delta Q$). In this case, the enhancement of the electron transition energy actually results in reduced capture kinetic barrier.

Second, the formation of O_I leads to a smaller lattice relaxation associated with the charge-state transition, as shown by a smaller ΔQ in the CCDs, compared with V_I, which reduces the kinetic barrier for the electron capture process further by moving the intersection of the PESs closer to the equilibrium configuration of O_I^0. Indeed, the PES of O_I^- almost goes through the minimum of the PES of the excited O_I^0, resulting in an extremely small electron capture barrier, rationalizing the counterintuitive enhancement of the electron capture process.

Furthermore, in the case of hole capture, both systems are within the Marcus inverted region. Compared with V_I, O_I reduces the hole transition energy and hence contributes to the enhancement of the capture barrier. On the other hand, the smaller lattice relaxation associated with the transition of $O_I^0 \leftrightarrow O_I^-$ contributes to the reduced hole capture barrier, which comparably alleviates the effect of the reduced transition energy. Consequently, V_I and O_I exhibit similar hole capture barriers and coefficients. However, they are not the rate-limiting steps for nonradiative recombination, and thus do not effectively impact the recombination rate.

The results suggest that to effectively suppress the nonradiative recombination and increase carrier lifetime in the $MASnI_3$-based devices in air, in addition to developing encapsulation technology to prevent environmental oxygen contamination, defect engineering to minimize the density of native I vacancies would be a critical step. In principle, synthesizing the material under I-rich conditions can inhibit the formation of V_I in $MASnI_3$ active layers. However, such growth conditions can also increase the density of V_{Sn}[17,18], which would result in severe *p*-type conductivity and thus impacts photovoltaic performance. This implies that the commonly used growth condition manipulation falls short of addressing the issue induced by intrinsic defects in $MASnI_3$, in stark contrast to that of Pb-based perovskites[16]. To further improve the performance of the related devices operating in the air, future research should focus on extrinsic anion engineering for suppressing the formation of V_I and alleviating *p*-type self-doping. Indeed, experiments show clues that appropriate extrinsic anion doping, such as Br^-, Cl^-, as well as the pseudo-halides of Ac^- (acetate) and $HCOO^-$ (formate), can efficiently decrease the density of deep traps and prolong the carrier lifetime in Sn-based perovskites[34–36]. V_I is filled by these anions, and the density of the detrimental O_I is effectively reduced, which is essential to enabling improved device performance. Our results provide a rationale for such enhancements.

Conclusion

In summary, based on first-principles hybrid DFT calculations, we have studied the mechanism of oxygen incorporation in accelerating carrier recombination in $MASnI_3$ and degrading the device performance. In $MASnI_3$, oxygen interstitials themselves are not responsible for nonradiative recombination. Rather, they tend to form the substitutional O_I by interacting strongly with the abundant native I vacancies (V_I) that are the dominant nonradiative recombination center in $MASnI_3$, and significantly enhance the original recombination rate from $9.3 \times 10^6\ s^{-1}$ to $1.8 \times 10^9\ s^{-1}$. Significantly, despite an enhancement in the electron transition energy (from 0.48 eV to 0.73 eV), the formation of O_I strengthens the lattice and reduces structural relaxation upon electron capture. These effects synergistically contribute to a higher electron capture coefficient, thus facilitating faster nonradiative carrier recombination in O_I. Our results thus point to a way to effectively suppress nonradiative recombination loss in

$MASnI_3$: in addition to preventing O ingression, minimizing the density of native V_I would be a critical step. These insights advance our understanding of how oxygen impacts the carrier dynamics and power conversion efficiency in $MASnI_3$-based devices, assisting in the future design and optimization of nontoxic Sn-based perovskite solar cells and other broad optoelectronics upon oxygen (ambient air) exposure.

Computational Method

The first-principles calculations in this work are performed based on density functional theory as implemented in the Vienna *ab initio* simulation package (VASP)[37]. The Heyd-Scurseria-Ernzerhof (HSE06) hybrid functional[38] including spin-orbit coupling (SOC) was employed with a kinetic energy cutoff of 400 eV. The Tkatchenko-Scheffler (TS) scheme[39] was adopted to describe the dispersion interactions and all the structures were fully relaxed until the forces on atoms are less than 0.01 eV/Å. The HSE mixing parameter was set to 0.43, yielding a bandgap of 1.19 eV for α-$MASnI_3$, consistent with the experiment of 1.20 eV[40]. The cell parameter is fixed to the experimental value of 6.23 Å[40]. For the defect calculations, a Monkhorst–Pack sampling of $2 \times 2 \times 2$ k-points was employed for the $2 \times 2 \times 2$ supercells with 96 atoms. The convergence test was further performed using a larger $3 \times 3 \times 2$ 216-atom supercell of $MASnI_3$. For the relevant V_I^- and O_I^- defects, the calculated formation energy differences between the 96-atom and 216-atom supercells are less than 0.08 eV.

The formation energy of a defect (D) with charge state (q) is calculated by the equation below[16]:

$$\Delta H^f\left(\mathrm{D}_\mathrm{i}^\mathrm{q}\right) = E\left(\mathrm{D}_\mathrm{i}^\mathrm{q}\right) - E(host) - \sum n_i(\mu_i + \Delta\mu_i) + q(E_F + E(VBM) + \Delta V) + \Delta_{corr}^{q} \quad (1)$$

where $E\left(\mathrm{D}_\mathrm{i}^\mathrm{q}\right)$ and $E(host)$ are ground-state total energies of the supercells with and without defects, respectively. n_i stands for the number of atoms added (removed) into the supercell to generate the defect. μ_i and $\Delta\mu_i$ are absolute and relative values of the chemical potential. The host chemical potentials were chosen according to the typical moderate growth condition, as shown in **Figure S1**. For the chemical potential of oxygen, we used half of the total energy of an isolated O_2, as a reference. E_f is the Fermi energy measured from the valance band maximum of the pristine system

$E(VBM)$. The correction term ΔV is used for ensuring the alignment of the potential for the charged defect in supercells and Δ_{corr}^{q} stands for the finite-size correction term for the periodic images of the charged defects[41].

With the formation energy of ΔH^f, the defect density at thermal equilibrium can be calculated by[16]: $N = N_0 e^{-\frac{\Delta Hf}{KT}}$, where N_0 stands for the number of available sites for defect formation per volume, and K the Boltzmann constant. Temperature (T) was set to room temperature.

The transition level is defined as the Fermi-level position for which the formation energies of different defect charge states are equal and thus is given by[16]:

$$\mathcal{E}(q/q') = \left[\Delta H^f\left(\mathrm{D_i^q}, E_F = 0\right) - \Delta H^f\left(\mathrm{D_i^{q'}}, E_F = 0\right)\right]/(q' - q) \quad (2)$$

The binding energy of the oxygen interstitial with the three types of native vacancies (x=I, Sn, and MA) is calculated by: $\Delta \mathrm{E} = \mathrm{E_{tot}(O_x)} - \mathrm{E_{tot}(V_x + O_i)}$, where $\mathrm{E_{tot}(O_x)}$ and $\mathrm{E_{tot}(V_x + O_i)}$ stands for the ground-state total energies of the systems with $\mathrm{O_i}$ residing in, and far away, from the native vacancies, respectively.

The nonradiative carrier capture coefficients were calculated using the established multiphonon emission methodology in conjunction with an extension to include the effect of lattice anharmonicity by solving the one-dimensional Schrodinger equation for the anharmonic potential energy surfaces[23,24]. The potential energy surfaces along the configuration coordinate are obtained by interpolating the energies from first-principles calculations. The electron−phonon coupling matrix elements for electron and hole capture are evaluated within the linear-coupling approximation based on the PAW results by VASP processed with the NONRAD package[23,24].

Reference

1. Jeong, J. *et al.* Pseudo-halide anion engineering for α-FAPbI 3 perovskite solar cells. *Nature* **592**, 381–385 (2021).
2. Min, H. *et al.* Perovskite solar cells with atomically coherent interlayers on SnO2

electrodes. *Nature* **598**, 444–450 (2021).

3. Kim, J. Y., Lee, J.-W., Jung, H. S., Shin, H. & Park, N.-G. High-Efficiency Perovskite Solar Cells. *Chem. Rev.* **120**, 7867–7918 (2020).
4. Cao, J. & Yan, F. Recent progress in tin-based perovskite solar cells. *Energy Environ. Sci.* **14**, 1286–1325 (2021).
5. Tai, Q. *et al.* Antioxidant Grain Passivation for Air-Stable Tin-Based Perovskite Solar Cells. *Angewandte Chemie International Edition* **58**, 806–810 (2019).
6. Mundt, L. E. *et al.* Surface-Activated Corrosion in Tin–Lead Halide Perovskite Solar Cells. *ACS Energy Lett.* **5**, 3344–3351 (2020).
7. Lanzetta, L. *et al.* Degradation mechanism of hybrid tin-based perovskite solar cells and the critical role of tin (IV) iodide. *Nat Commun* **12**, 2853 (2021).
8. Zhang, Z. *et al.* Revealing superoxide-induced degradation in lead-free tin perovskite solar cells. *Energy Environ. Sci.* **15**, 5274–5283 (2022).
9. Li, H. *et al.* Surface Reconstruction for Tin-Based Perovskite Solar Cells. *ACS Energy Lett.* **7**, 3889–3899 (2022).
10. Luo, D., Su, R., Zhang, W., Gong, Q. & Zhu, R. Minimizing non-radiative recombination losses in perovskite solar cells. *Nat. Rev. Mater.* **5**, 44–60 (2020).
11. Zhang, X., Shen, J.-X. & Van de Walle, C. G. First-Principles Simulation of Carrier Recombination Mechanisms in Halide Perovskites. *Advanced Energy Materials* **10**, 1902830 (2020).
12. Liu, X. *et al.* Efficient and stable tin perovskite solar cells enabled by amorphous-polycrystalline structure. *Nat Commun* **11**, 2678 (2020).
13. Ke, W. *et al.* Enhanced photovoltaic performance and stability with a new type of hollow 3D perovskite {en}FASnI3. *Science Advances* **3**, e1701293 (2017).
14. Yao, H. *et al.* Strategies for Improving the Stability of Tin-Based Perovskite

(ASnX3) Solar Cells. *Advanced Science* **7**, 1903540 (2020).

15. Shockley, W. & Read, W. T. Statistics of the Recombinations of Holes and Electrons. *Phys. Rev.* **87**, 835–842 (1952).
16. Kang, J., Li, J. & Wei, S.-H. Atomic-scale understanding on the physics and control of intrinsic point defects in lead halide perovskites. *Applied Physics Reviews* **8**, 031302 (2021).
17. Meggiolaro, D., Ricciarelli, D., Alasmari, A. A., Alasmary, F. A. S. & De Angelis, F. Tin versus Lead Redox Chemistry Modulates Charge Trapping and Self-Doping in Tin/Lead Iodide Perovskites. *J. Phys. Chem. Lett.* **11**, 3546–3556 (2020).
18. Shi, T. *et al.* Effects of organic cations on the defect physics of tin halide perovskites. *J. Mater. Chem. A* **5**, 15124–15129 (2017).
19. Zhang, X., Turiansky, M. E., Shen, J.-X. & Van de Walle, C. G. Iodine interstitials as a cause of nonradiative recombination in hybrid perovskites. *Phys. Rev. B* **101**, 140101 (2020).
20. Meggiolaro, D. & De Angelis, F. First-Principles Modeling of Defects in Lead Halide Perovskites: Best Practices and Open Issues. *ACS Energy Lett.* **3**, 2206–2222 (2018).
21. Whalley, L. D. *et al.* Giant Huang–Rhys Factor for Electron Capture by the Iodine Intersitial in Perovskite Solar Cells. *J. Am. Chem. Soc.* **143**, 9123–9128 (2021).
22. Liang, Y. *et al.* Hydrogen-Anion-Induced Carrier Recombination in MAPbI3 Perovskite Solar Cells. *J. Phys. Chem. Lett.* **12**, 10677–10683 (2021).
23. Alkauskas, A., Yan, Q. & Van de Walle, C. G. First-principles theory of nonradiative carrier capture via multiphonon emission. *Phys. Rev. B* **90**, 075202 (2014).
24. Turiansky, M. E. *et al.* Nonrad: Computing nonradiative capture coefficients from

first principles. *Comput. Phys. Commun.* **267**, 108056 (2021).

25. Agiorgousis, M. L., Sun, Y.-Y., Zeng, H. & Zhang, S. Strong Covalency-Induced Recombination Centers in Perovskite Solar Cell Material $CH_3NH_3PbI_3$. *J. Am. Chem. Soc.* **136**, 14570–14575 (2014).
26. Wang, J., Li, W. & Yin, W. Passivating Detrimental DX Centers in $CH_3NH_3PbI_3$ for Reducing Nonradiative Recombination and Elongating Carrier Lifetime. *Adv. Mater.* **32**, 1906115 (2020).
27. Alkauskas, A., Dreyer, C. E., Lyons, J. L. & Van de Walle, C. G. Role of excited states in Shockley-Read-Hall recombination in wide-band-gap semiconductors. *Phys. Rev. B* **93**, 201304 (2016).
28. Euvrard, J., Yan, Y. & Mitzi, D. B. Electrical doping in halide perovskites. *Nat Rev Mater* **6**, 531–549 (2021).
29. Johnston, M. B. & Herz, L. M. Hybrid Perovskites for Photovoltaics: Charge-Carrier Recombination, Diffusion, and Radiative Efficiencies. *Acc. Chem. Res.* **49**, 146–154 (2016).
30. Noel, N. K. *et al.* Lead-free organic–inorganic tin halide perovskites for photovoltaic applications. *Energy Environ. Sci.* **7**, 3061–3068 (2014).
31. Tai, Q., Cao, J., Wang, T. & Yan, F. Recent advances toward efficient and stable tin-based perovskite solar cells. *EcoMat* **1**, e12004 (2019).
32. Henry, C. H. & Lang, D. V. Nonradiative capture and recombination by multiphonon emission in GaAs and GaP. *Phys. Rev. B* **15**, 989–1016 (1977).
33. Suppan, P. The marcus inverted region. in *Photoinduced Electron Transfer IV* (ed. Mattay, J.) 95–130 (Springer, 1992). doi:10.1007/3-540-55117-4_5.
34. Zhu, H. *et al.* High-performance hysteresis-free perovskite transistors through anion engineering. *Nat Commun* **13**, 1741 (2022).

35. Qiu, J., Xia, Y., Chen, Y. & Huang, W. Management of Crystallization Kinetics for Efficient and Stable Low-Dimensional Ruddlesden–Popper (LDRP) Lead-Free Perovskite Solar Cells. *Advanced Science* **6**, 1800793 (2019).
36. Liang, C. *et al.* Two-dimensional Ruddlesden–Popper layered perovskite solar cells based on phase-pure thin films. *Nat Energy* **6**, 38–45 (2021).
37. Kresse, G. & Furthmüller, J. Efficiency of ab-initio total energy calculations for metals and semiconductors using a plane-wave basis set. *Comput. Mater. Sci.* **6**, 15–50 (1996).
38. Heyd, J., Scuseria, G. E. & Ernzerhof, M. Erratum: "Hybrid functionals based on a screened Coulomb potential" [J. Chem. Phys. 118, 8207 (2003)]. *The Journal of Chemical Physics* **124**, 219906 (2006).
39. Tkatchenko, A. & Scheffler, M. Accurate Molecular Van Der Waals Interactions from Ground-State Electron Density and Free-Atom Reference Data. *Phys. Rev. Lett.* **102**, 073005 (2009).
40. Stoumpos, C. C., Malliakas, C. D. & Kanatzidis, M. G. Semiconducting Tin and Lead Iodide Perovskites with Organic Cations: Phase Transitions, High Mobilities, and Near-Infrared Photoluminescent Properties. *Inorg. Chem.* **52**, 9019–9038 (2013).
41. Freysoldt, C., Neugebauer, J. & Van de Walle, C. G. Fully Ab Initio Finite-Size Corrections for Charged-Defect Supercell Calculations. *Phys. Rev. Lett.* **102**, 016402 (2009).